

A phenomenological-based dynamic model of ethanol steam reforming for hydrogen production

Abstract

This article presents a detailed deduction of a nonlinear dynamic model for an ethanol steam reforming (ESR) process designed to produce pure hydrogen for fuel-cell applications and renewable energy integration. Such a model is derived by using a well-established phenomenological-based semi-physical modeling (PBSM) methodology. The process comprises two sequential stages, the reforming stage and the hydrogen separation stage, both carried out within a single integrated module known as a staged-separation membrane reactor (SSMR). The resulting system of algebraic and ordinary differential equations captures the temporal and spatial evolution of gas temperature and species concentrations along the device, effectively representing the system's dynamics. A set of model parameters are identified using a multi-objective optimization algorithm to fit the model to experimental data obtained from a real SSMR setup. Simulation results under various operating conditions demonstrate the model accuracy and reliability. The model is implemented in Python and is openly accessible through an online repository.

Keywords: nonlinear dynamic model, ethanol steam reforming, hydrogen production, staged-separation membrane reactor, renewable energy

1. Introduction

Modern societies are experiencing an ever-growing demand for energy to support economic development, technological advancement, and enhanced quality of life [1]. Despite progress in energy efficiency and renewable technologies, conventional energy production and consumption remain the primary sources of greenhouse gas emissions [2], contributing to climate change and generating significant environmental and ecological challenges [3]. In response, governments, industries, and research communities worldwide are

intensifying efforts to transition toward sustainable energy systems, aiming to reduce carbon footprints and meet international climate commitments [4, 5].

Among the strategies to achieve these sustainability goals, the development of renewable energy technologies plays a central role. Solar, wind, and biomass-based systems have demonstrated considerable potential to reduce greenhouse gas emissions [6]. However, their intermittent nature and storage limitations require complementary solutions for energy management [7]. In this context, hydrogen has emerged as a versatile and promising energy carrier, capable of bridging the gap between variable renewable energy sources and stable energy demand [8, 9]. Its advantages include high energy density, suitability for long-term storage, potential for clean power generation, and compatibility with existing infrastructure when appropriately managed [10, 11].

The sustainability of hydrogen depends critically on the production pathway [12, 13]. Currently, the majority of global hydrogen is produced via fossil fuel-based processes [14], particularly natural gas reforming, which generates substantial greenhouse gas emissions and undermines the environmental benefits of hydrogen utilization. To overcome this limitation, cleaner production routes are being actively explored [15, 16]. Water electrolysis powered by renewable electricity represents a low-carbon alternative [17, 18, 19], but its widespread deployment is constrained by technological challenges, including efficiency limitations, high material costs, and durability concerns [20, 21].

As a complementary approach, steam reforming of short-chain alcohols, particularly methanol and ethanol, has attracted considerable attention [22]. These alcohols offer high hydrogen-to-carbon ratios and can be derived from biomass. Moreover, since alcohols are relatively easy to handle, store, and transport, hydrogen production can be decentralized or carried out on-demand at points of use [23]. Alcohol steam reforming (ASR) involves catalytic reactions of alcohol with steam under external heat input, producing hydrogen along with minor byproducts [24]. When the heat source is renewable, ASR provides a pathway for low-carbon hydrogen production that can be integrated with existing energy systems, contributing directly to decarbonization strategies and sustainable energy goals. Unlike electrolysis, ASR does not require large-scale electricity inputs, which can be advantageous in regions where renewable electricity is either intermittent or limited.

The practical implementation of ASR processes requires reliable mathematical models capable of effectively capturing the system's dynamics. Phenomenological-based modeling enables the representation of complex sys-

tems through physically meaningful equations, providing insights into reaction mechanisms, transport phenomena, temporal and spatial dynamics, and the effects of operating conditions on process performance [25]. These models are essential for the design, scale-up, and control of hydrogen production units, as they support experimental planning, guide industrial implementation, and help address key operational challenges such as catalyst deactivation from carbon deposition, management of harmful byproducts for downstream fuel cells, and the optimization of heat and mass transfer within the reactor.

A substantial portion of ASR research has focused on optimizing catalyst properties to enhance process performance [26, 27], as well as examining thermodynamic aspects, reaction mechanisms, reactor configurations, and key variables that influence the efficient production of hydrogen [28, 29]. Another group of studies focuses on gaining insights into the system through modeling. For instance, [30] explores advancements in hydrogen production through steam reforming of bio-alcohols, particularly methanol and ethanol, utilizing membrane-assisted reactors and artificial intelligence modeling techniques. It emphasizes the significance of operational parameters such as feed composition, temperature, and pressure on hydrogen recovery and conversion rates. Likewise, [31] develops a fully 3D non-isothermal computational fluid dynamics (CFD) model to simulate the ethanol steam reforming (ESR) process over Rh–Pd/CeO₂ catalytic honeycombs, which allows for the analysis of heat transfer and reaction extent under various operating conditions.

The authors in [32] highlight the role of various catalysts and reactor designs, particularly in membrane-assisted packed bed reactors. Utilizing multiscale modeling and CFD simulations, the research investigates the effects of internal diffusion and membrane separation on reaction rates and hydrogen yield. Key findings reveal that optimizing catalyst particle size and porosity can significantly enhance reforming efficiency. Besides, [33] presents a comprehensive study on the design and numerical modeling of microchannel reactors for hydrogen production through methanol steam reforming (MSR). Such a paper presents a mathematical model that incorporates conservation equations and chemical kinetics, addressing complex catalyst dynamics and transport phenomena. The findings highlight the impact of various parameters such as washcoat thickness, catalyst loading, and flow rates on hydrogen production efficiency, emphasizing the advantages of microchannel technology in enhancing reaction rates and selectivity. Similarly, [34] investigates how different channel structures in embedded reactors influence MSR

performance. Using heat and mass transfer analysis, it shows that the circle–triangle channel achieves the highest efficiency, offering valuable insights for optimizing reactor design. Finally, the study in [35] evaluates crossflow membrane reactors for ESR and water-gas shift reactions, showing that Pd-based membranes and optimized designs significantly enhance hydrogen production and separation, demonstrating strong potential for efficient reactor performance.

Despite the aforementioned approaches and others reported in the literature, no work has been found that focuses on the detailed deduction and validation of a mathematical model for ASR. Hence, the main contribution of this article is to fully derive and validate a mathematical model of ESR through a well-established phenomenological-based semi-physical modeling (PBSM) methodology [36]. The PBSM approach comprises ten defined steps that yield mathematical models blending characteristics of both white-box and black-box models. In other words, the basic structure of the model is completely derived from first principles, but the model also includes some parameters that can be adjusted based on experimental data. This methodology has been successfully applied to generate models across various applications, as the well-described models in [37, 38].

The remainder of this article is outlined as follows: Section 2 presents the model pre-construction, where the system is described. Then, the model equations are derived in Section 3 in the model construction. Section 4 provides the model simulation and validation and, finally, the main conclusions of this work are drawn in Section 5.

2. Model pre-construction

In this section, the first three steps of the PBSM methodology are applied to the whole system.

2.1. Step 1. Process description and modeling objective

The process involves the production of pure hydrogen via ESR, comprising two consecutive stages: reforming and hydrogen separation. Both stages take place within a single operating unit, the SSMR, which is depicted in the schematic of Fig. 1. The reforming stage consists of a honeycomb (400 cells per square inch) monolithic reactor with cobalt-based catalytic walls. This type of reactor provides a high surface area compared to its volume. Besides, the narrow channels of the monoliths offer a short radial path between the

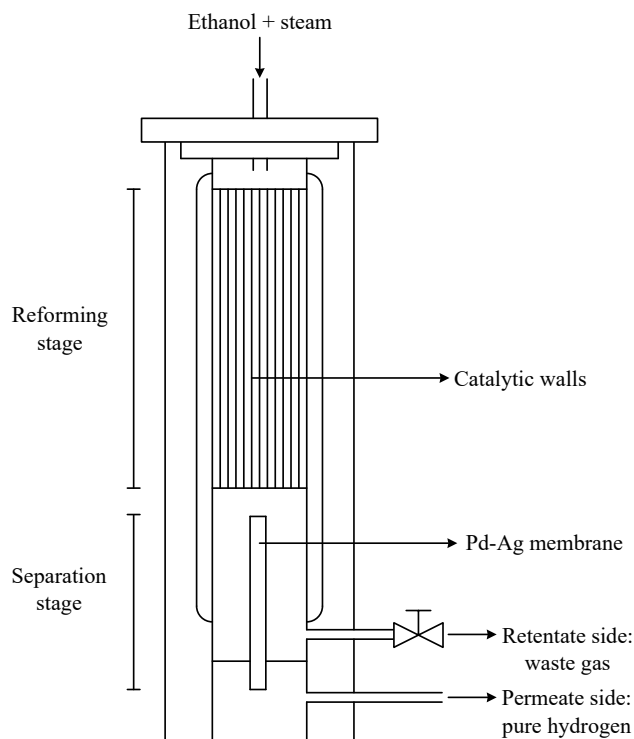
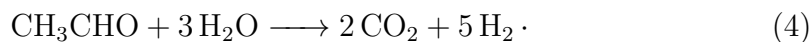
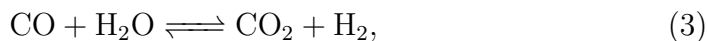
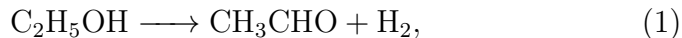


Fig. 1. Schematic representation of the staged-separation membrane reactor (SSMR).

gas phase and the solid surface, which reduces the possibility of mass transfer limitations. Ethanol and water are fed into the reactor as vapors after passing through a heating conduit that preheats the mixture before entering into the device.

Inside the reactor, the following four reactions take place in the same space and conditions simultaneously:



Ethanol dehydrogenates into acetaldehyde and hydrogen (1). In parallel, an undesired reaction occurs in which ethanol is decomposed into carbon monoxide, methane, and hydrogen (2). The cobalt-based catalyst also promotes the water-gas shift (WGS) reaction (3) under typical operating conditions.

Meanwhile, acetaldehyde is further reformed with water into carbon dioxide and hydrogen (4). Since the whole reaction system is highly endothermic, the SSMR is externally heated by using an electric resistance heater to maintain the operating temperature. Hereafter, chemical species are denoted by their corresponding initial letters, i.e., ethanol (E), acetaldehyde (A), hydrogen (H), water (W), carbon dioxide (CD), carbon monoxide (CM), and methane (M).

In the separation stage, only hydrogen permeates through a palladium-silver (Pd-Ag) membrane. The selective permeability of the membrane allows hydrogen atoms to pass through while effectively blocking other gases present in the gas stream. As a result, pure hydrogen is obtained at the permeate side, while the remaining gases are extracted from the retentate side. The objective of the mathematical model is to predict how the temperature and species concentrations evolve over time along the axial direction of the SSMR.

2.2. Step 2. Modeling hypothesis and level of detail

For this case study, the modeling hypothesis aligns with that of a plug flow reactor (PFR). While the reactants flow through the reactor, the concentrations, temperature, and reaction rates change. At a macroscopic level, the reactants predominantly flow axially through the internal channels of the monolith. However, at a mesoscopic level, radial transport of reactants takes place towards the boundary layer adhered to the monolith walls containing the solid catalyst. From the bulk of the gas phase, there is mass transfer of reactants to the walls surface, where they are adsorbed into the catalytic active sites. Then, the reactions (1)-(4) occur, followed by desorption of the products to the boundary layer, after which these reaction products are transferred to the bulk of the gas phase (see the schematic in Fig. 2).

The reaction products, along with any unreacted species, leave the reforming stage and proceed to the separation stage. There, through a solution-diffusion mechanism [39], hydrogen permeation begins as hydrogen molecules arrive at one side of the membrane, where they dissociate into atomic hydrogen upon interaction with its surface. Then, these atoms dissolve into the metal structure of the membrane. Following dissolution, hydrogen atoms diffuse through the metal driven by the partial pressure gradient across the membrane. Finally, hydrogen atoms recombine on the permeate side to form molecular hydrogen gas again.

To formulate the SSMR model, both the reforming and separation stages are discretized into n slices or partitions along the axis flow direction. The

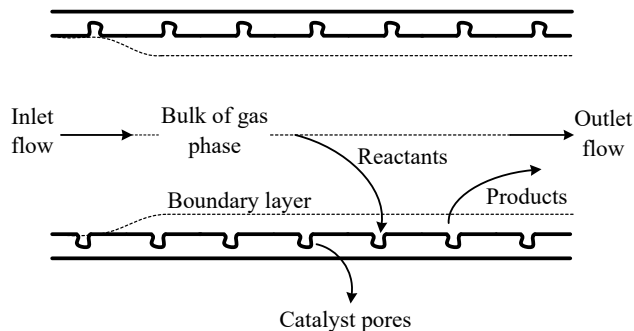


Fig. 2. Overall representation of the process phenomena occurring along one channel in the reforming stage.

phenomena involved in the process are modeled on a macroscopic scale, as each predefined slice holds a macroscopic order of magnitude (a few millimeters). Partitioning the reactor into slices results in a distributed-parameters system, i.e., each slice has its own parameters. However, perfect agitation is assumed within each partition, resulting in a lumped-parameters model for each slice. This assumption remains also valid in the separation stage. Additional assumptions complementing the modeling hypothesis are stated as follows:

- The similarity of the channels in the monolith allows them to have the same hydrodynamic and chemical behavior. Thus, modeling just one channel in the reforming stage is enough to achieve the modeling objective.
- The ideal gas equation is applicable within the operating pressure range within the device. This assumption is valid for the relatively low pressures that are typically found in SSMR.
- The radial dependence of pressure and temperature is negligible in both the ESR and membrane separation. The former assumption is reasonable because there is no relevant radial flow or friction, while the latter is justified by the short length scale in the radial direction compared to the axial direction.
- The velocity dependence in the radial direction is neglected. Instead, the velocity is taken to be average velocity in the axial direction.

- The effects of molecular diffusion in the axial direction are negligible with respect to convection in this direction. The suitability of this assumption is confirmed by calculation of the Péclet number.
- No accumulation of substances occurs in any of the partitions or in the boundary layer, e.g., effects as the catalyst poisoning are not considered in this version of the model.
- The wall temperature of the separation stage and all channels within the monolith is assumed to remain uniform and constant throughout the device. This assumption is justified by the implementation of a control system in the real SSMR setup, which efficiently regulates this temperature.

2.3. Step 3. Process systems definition

A process system (PS) is an arbitrary abstraction of a specific part of the process, which is treated as an individual system. Hence, it is possible to apply all the available methods for system analysis [40]. An important clue to identify PSs is to locate physical separations or boundaries within the process, as well as distinguishable phase changes or mass characteristics pointing out spatial differences. According to the modeling objective, species concentrations and gas temperature need to be monitored continuously as chemical species pass through the reforming stage, move into the separation stage, and leave the SSMR. Therefore, the following PSs, which can be seen in Fig. 3, are considered:

- Process system I (PS I). It includes the gas phase, comprising both the bulk flow and the gas within the boundary layer and catalyst pores in the reforming stage.
- Process system II (PS II). It represents the gas phase that flows through the retentate side of the membrane.
- Process system III (PS III). It consists of the gas phase contained in the permeate side of the membrane. This PS is composed of the pure hydrogen coming from PS II.

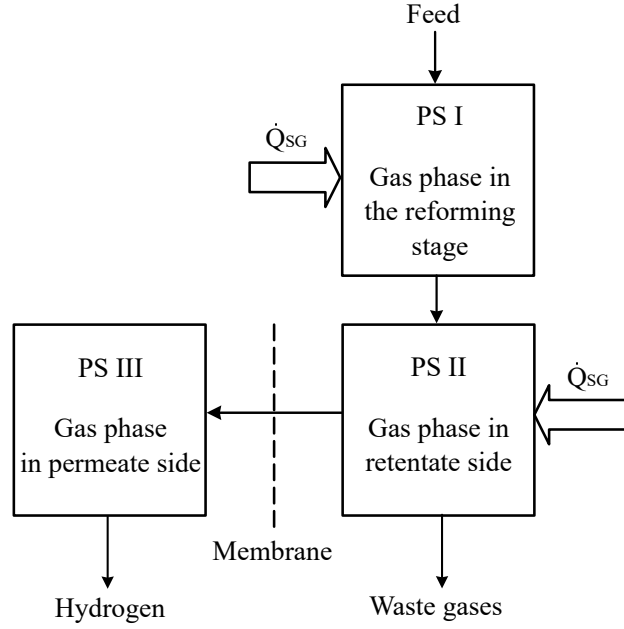


Fig. 3. Process systems (PSs) defined for the model deduction. Thin arrows represent flow of material, while thick arrows indicate flow of energy.

3. Model construction

In this section, steps 4 to 7 of the modeling methodology are applied. All the model equations are provided here.

3.1. Step 4. Conservation principle application

In this step, dynamic material and energy balances are formulated for each PS in order to determine the basic structure of the model. It should be noted that the derived set of equations must be applied to each partition, namely z , individually. By continuity, the output conditions of one partition correspond to the input conditions of the subsequent partition.

3.1.1. Process system I

The total material balance for this PS, in molar units, is formulated as

$$\frac{dN_{G,I}}{dt} = \dot{n}_{z-1} + \sum_{i=E}^M \sum_{j=1}^4 v_{i,j} r_j - \dot{n}_z, \quad (5)$$

where $N_{G,I}$ represents the total gas moles in partition z within PS I, $t \in \mathbb{R}_{\geq 0}$ is the time, \dot{n}_{z-1} is the total molar flow rate coming from partition $z - 1$, and \dot{n}_z is the total molar flow rate leaving the current partition z . Moreover, $v_{i,j}$ is the stoichiometric coefficient of compound $i \in \{E, A, H, W, CD, CM, M\}$ in reaction $j \in \{1, 2, 3, 4\}$ and r_j is the rate of reaction j . On the other hand, the component material balance, in terms of molar fraction, is derived below for ethanol. For the other substances, only the final expression is shown.

Ethanol (E):

$$\frac{dN_{E,I}}{dt} = y_{E,z-1} \dot{n}_{z-1} - r_1 - r_2 - y_{E,z} \dot{n}_z, \quad (6)$$

where $N_{E,I}$ denotes the moles of ethanol in partition z within PS I, $y_{E,z-1}$ and $y_{E,z}$ represent the mole fraction of ethanol in partitions $z - 1$ and z , respectively. Likewise, r_1 and r_2 are the rates of reactions 1 and 2, respectively. Then, by substituting the moles of ethanol with the product of the mole fraction of ethanol and the total moles of gas in the respective partition, and computing the derivative of this product, the following equation is obtained:

$$y_{E,z} \frac{dN_{G,I}}{dt} + N_{G,I} \frac{dy_{E,z}}{dt} = y_{E,z-1} \dot{n}_{z-1} - r_1 - r_2 - y_{E,z} \dot{n}_z, \quad (7)$$

in which the derivative of $N_{G,I}$ with respect to time can be represented as a parameter denoted $\dot{N}_{G,I}$. This parameter is directly obtained from the right-hand side of (5) at any moment, but taking it as an algebraic equation. Finally, solving for the derivative of the mole fraction of ethanol with respect to time, the final expression is

$$\frac{dy_{E,z}}{dt} = \frac{1}{N_{G,I}} \left(y_{E,z-1} \dot{n}_{z-1} - r_1 - r_2 - y_{E,z} \dot{n}_z - y_{E,z} \dot{N}_{G,I} \right). \quad (8)$$

The previous component balance results similar for each substance involved in the process, but with adjustments made to terms specific to chemical reactions, that is,

Acetaldehyde (A):

$$\frac{dy_{A,z}}{dt} = \frac{1}{N_{G,I}} \left(y_{A,z-1} \dot{n}_{z-1} + r_1 - r_4 - y_{A,z} \dot{n}_z - y_{A,z} \dot{N}_{G,I} \right). \quad (9)$$

Hydrogen (H):

$$\frac{dy_{H,z}}{dt} = \frac{1}{N_{G,I}} \left(y_{H,z-1} \dot{n}_{z-1} + r_1 + r_2 + r_3 + 5r_4 - y_{H,z} \dot{n}_z - y_{H,z} \dot{N}_{G,I} \right). \quad (10)$$

Water (W):

$$\frac{dy_{W,z}}{dt} = \frac{1}{N_{G,I}} \left(y_{W,z-1} \dot{n}_{z-1} - r_3 - 3r_4 - y_{W,z} \dot{n}_z - y_{W,z} \dot{N}_{G,I} \right). \quad (11)$$

Carbon dioxide (CD):

$$\frac{dy_{CD,z}}{dt} = \frac{1}{N_{G,I}} \left(y_{CD,z-1} \dot{n}_{z-1} + r_3 + 2r_4 - y_{CD,z} \dot{n}_z - y_{CD,z} \dot{N}_{G,I} \right). \quad (12)$$

Carbon monoxide (CM):

$$\frac{dy_{CM,z}}{dt} = \frac{1}{N_{G,I}} \left(y_{CM,z-1} \dot{n}_{z-1} + r_2 - r_3 - y_{CM,z} \dot{n}_z - y_{CM,z} \dot{N}_{G,I} \right). \quad (13)$$

Methane (M):

$$\frac{dy_{M,z}}{dt} = \frac{1}{N_{G,I}} \left(y_{M,z-1} \dot{n}_{z-1} + r_2 - y_{M,z} \dot{n}_z - y_{M,z} \dot{N}_{G,I} \right). \quad (14)$$

The energy balance in PS I accounts for the energy exchanged in the specific partition z , including the mass entering and leaving the partition, as well as the heat exchanged with the surroundings, that is,

$$\begin{aligned} \frac{dE_{G,I}}{dt} &= \frac{d(N_{G,I} \bar{C}_v T_{G,z})}{dt} \\ &= \dot{n}_{z-1} \bar{H}_{z-1} - \sum_{j=1}^4 r_j \Delta \bar{H}_{\text{rxn},j} - \dot{n}_z \bar{H}_z + \dot{Q}_{SG}, \end{aligned} \quad (15)$$

with $E_{G,I}$ being the gas thermal energy, \bar{C}_v being the average molar heat capacity of the gas at constant volume, and $T_{G,z}$ being the gas temperature in partition z . Likewise, \bar{H}_{z-1} and \bar{H}_z represent the gas molar enthalpy in partition $z-1$ and partition z , respectively. Moreover, $\Delta \bar{H}_{\text{rxn},j}$ is the molar enthalpy of reaction j and \dot{Q}_{SG} represents the heat flow from the solid to the

gas inside the channel. Then, assuming constant heat capacity, computing the derivative of the product $N_{G,I} T_{G,z}$ and solving for the derivative of $T_{G,z}$, the final energy balance equation is expressed as follows:

$$\frac{dT_{G,z}}{dt} = \frac{1}{\bar{C}_v N_{G,I}} \left(\dot{n}_{z-1} \bar{H}_{z-1} - \sum_{j=1}^4 r_j \Delta \bar{H}_{\text{rxn},j} - \dot{n}_z \bar{H}_z + \dot{Q}_{SG} \right) - \frac{T_{G,z}}{N_{G,I}} \dot{N}_{G,I}. \quad (16)$$

3.1.2. Process system II

The total material balance, in molar units, is expressed as

$$\frac{dN_{G,II}}{dt} = \dot{n}_{z-1} - \dot{n}_{H,z} - \dot{n}_z, \quad (17)$$

where $N_{G,II}$ represents the total gas moles in partition z within PS II and $\dot{n}_{H,z}$ is the molar flow rate of hydrogen permeating through the membrane in the current partition. On the other hand, since there are no chemical reactions in the separation stage, the component material balance is straightforward for the remaining compounds that do not permeate the membrane, that is,

$$\frac{dy_{i,z}}{dt} = \frac{1}{N_{G,II}} \left(y_{i,z-1} \dot{n}_{z-1} - y_{i,z} \dot{n}_z - y_{i,z} \dot{N}_{G,II} \right), \quad (18)$$

where $\dot{N}_{G,II}$ is a parameter denoting the change of $N_{G,II}$ with respect to time, which is directly extracted from the right-hand side of (17), taken as an algebraic equation, and $i \in \{E, A, W, CD, CM, M\}$. Instead, the component material balance for hydrogen is written as follows:

$$\frac{dy_{H,z}}{dt} = \frac{1}{N_{G,II}} \left(y_{H,z-1} \dot{n}_{z-1} - \dot{n}_{H,z} - y_{H,z} \dot{n}_z - y_{H,z} \dot{N}_{G,II} \right). \quad (19)$$

The energy balance for PS II is similar to that of PS I, but excluding the energy associated with chemical reactions and including an additional term accounting for the energy carried by the permeating hydrogen, as follows:

$$\frac{dT_{G,z}}{dt} = \frac{1}{\bar{C}_v N_{G,II}} \left(\dot{n}_{z-1} \bar{H}_{z-1} - \dot{n}_{H,z} \bar{H}_H - \dot{n}_z \bar{H}_z + \dot{Q}_{SG} \right) - \frac{T_{G,z}}{N_{G,II}} \dot{N}_{G,II}, \quad (20)$$

with \bar{H}_H being the molar enthalpy of hydrogen.

3.1.3. Process system III

In this PS, the total material balance is equivalent to the component material balance, as hydrogen is the only species present. Such a balance is expressed as

$$\frac{dN_{G,III}}{dt} = \dot{n}_{z-1} + \dot{n}_{H,z} - \dot{n}_z, \quad (21)$$

where $N_{G,III}$ represents the moles of hydrogen in partition z within PS III, \dot{n}_{z-1} is the molar flow rate of hydrogen coming from partition $z - 1$, and \dot{n}_z is the molar flow rate of hydrogen leaving the current partition z in PS III. On the other hand, since PS III is physically surrounded by PS II, no chemical reactions occur, and the thermal effects of the thin membrane are neglected, it is assumed that PS III remains in thermal equilibrium with PS II. Therefore, an energy balance for PS III is not required.

3.2. Step 5. Basic structure of the model

The basic structure of the mathematical model consists of the set of balance equations that provide relevant information to meet the modeling objective. In this case, such expressions are the equations from (5) to (21). It is important to highlight that (18) yields six equations, one for each compound involved in the process, except for hydrogen.

3.3. Step 6. Variables, parameters and constants

The basic structure of the mathematical model can include variables, parameters, and constants. In this article, variables are those which are determined only after simulating the model. Instead, parameters are unknowns for the set of model equations that must be defined, through constitutive and assessment equations, before simulating the model. Besides, constants are well-known fixed values, which are not subject to change. These parameters and constants are referred to as structural, since they appear explicitly in the equations forming the basic structure of the model. In this sense, the model variables and structural parameters and constants are reported in Table 1.

3.4. Step 7. Constitutive and assessment equations

This step focuses on defining the highest number of structural parameters using constitutive or assessment equations. If no such equations are available, parameters must be obtained from experimental data or estimated through correlation expressions. Since these parameters are directly observable from

Table 1. Model variables and structural parameters and constants.

PS	Variables	Structural parameters	Structural constants
I	$N_{G,I}$ $y_{E,z}$ $y_{A,z}$ $y_{H,z}$ $y_{W,z}$ $y_{CD,z}$ $y_{CM,z}$ $y_{M,z}$ $T_{G,z}$	\dot{n}_{z-1} \dot{n}_z r_j $\dot{N}_{G,I}$ \bar{C}_v $\Delta\bar{H}_{\text{rxn},j}$ \dot{Q}_{SG} \bar{H}	$v_{i,j}$
II	$N_{G,II}$ $y_{E,z}$ $y_{A,z}$ $y_{H,z}$ $y_{W,z}$ $y_{CD,z}$ $y_{CM,z}$ $y_{M,z}$ $T_{G,z}$	\dot{n}_{z-1} \dot{n}_z $\dot{n}_{H,z}$ $\dot{N}_{G,II}$ \bar{C}_v \bar{H}_H \dot{Q}_{SG} \bar{H}	-
III	$N_{G,III}$	\dot{n}_{z-1} \dot{n}_z $\dot{n}_{H,z}$	-

the material and energy balances comprising the basic structure of the model, they are inherently interpretable, which enhances their identification [41]. Sometimes, defining one structural parameter introduces additional parameters, called *functional* parameters, which also need to be specified. These new functions and parameters make up the extended structure of the model and must be clearly defined to maintain the logical sequence of the model formulation.

One of the most relevant features of the dynamic models derived by using the PBSM methodology is their modularity, i.e., they can be understood as the integration of several interacting processes. Consequently, the extended structure of the model can be expanded or simplified at any stage, depending on the available knowledge of the process and the modeling objectives. For instance, Appendix A discusses how mass transfer limitations, specifically those between the bulk gas and the gas in the boundary layer in the reforming stage, can be incorporated when required. In the following, some constitutive and assessment equations are presented, while the remaining ones are listed in Table 2.

Total molar flow rate \dot{n}_z . This parameter must be evaluated according to the specific PS and the partition for which it is calculated. In this case study, the partition $z = 0$ corresponds to the inlet of the reforming stage. Hence, \dot{n}_0 is obtained from the inlet molar flow rates of ethanol and steam, which are pre-defined values according to the operating conditions of the device. For the remaining partitions, the total molar flow rate is calculated as follows:

$$\dot{n}_z = \dot{n}_{z-1} + r_{1,z} + 2 r_{2,z} + 3 r_{4,z} \quad \text{for PS I,} \quad (22)$$

$$\dot{n}_z = \dot{n}_{z-1} - \dot{n}_{H,z} \quad \text{for PS II,} \quad (23)$$

$$\dot{n}_z = \dot{n}_{z-1} + \dot{n}_{H,z} \quad \text{for PS III.} \quad (24)$$

Reaction rates r_j . The reaction rates are determined as [42]

$$r_1 = k_1 \frac{p_E}{\alpha_1 + \beta_1(P_G - 1)}, \quad (25)$$

$$r_2 = k_2 p_E, \quad (26)$$

$$r_3 = k_3 \left(p_{CMPW} - \frac{p_{CDPH}}{k_{WGS}} \right), \quad (27)$$

$$r_4 = k_4 p_A p_W^3, \quad (28)$$

$$k_{WGS} = \exp \left(\frac{4577.8}{T_G} - 4.33 \right), \quad (29)$$

$$k_j = k_{\infty,j} \exp \left(-E_{a,j} \left(\frac{1}{RT_G} - \frac{1}{RT_{\text{ref}}} \right) \right), \quad (30)$$

in which k_j is the kinetic parameter of the j -th chemical reaction, α_1 and β_1 are parameters accounting for equilibrium effects, p_i is the partial pressure in bar of the i -th species, R is the gas universal constant, and k_{WGS} is a characteristic parameter of the water–gas shift reaction. Likewise, $k_{\infty,j}$ is the pre-exponential factor of the j -th kinetic parameter, $E_{a,j}$ is the activation energy of the j -th chemical reaction, and T_{ref} is the reference temperature for the reaction rates (expressions from (25) to (30)), which is set to¹ 773.15 K. The reaction rate r_1 is modified here to account for the effect of the operating total gas pressure P_G . Namely, additional terms were introduced in the denominator compared to the original expression from [42].

Partial pressures p_i . The partial pressures of the corresponding chemical species are easily obtained from the mole fraction of each compound and the total gas pressure, that is,

$$p_i = y_i P_G \times 10^{-5}. \quad (31)$$

Molar flow rate of permeating hydrogen \dot{n}_H . This molar flow rate arises from the mass transfer of hydrogen from PS II to PS III across the membrane.

¹773.15 K is the temperature of reference to be used for calculating the kinetic parameters of the chemical reactions, as indicated by the authors in [42]. It represents the nominal temperature at which such parameters were originally determined.

The process can be described by Sieverts' law [43], as follows:

$$\dot{n}_H = \frac{P_e}{\delta} \alpha (\sqrt{p_{H,r}} - \sqrt{p_{H,p}}), \quad (32)$$

$$P_e = P_{e,0} \exp\left(\frac{-E_{am}}{RT_G}\right), \quad (33)$$

where P_e is the permeability of the membrane, δ is the membrane thickness, α is the surface area of the membrane, and $p_{H,r}$ and $p_{H,p}$ are the hydrogen partial pressures at the retentate and permeate sides, respectively. Besides, $P_{e,0}$ is the permeability pre-exponential factor and E_{am} is the apparent activation energy of the membrane.

Molar enthalpy of gas \bar{H} . The molar enthalpy of the gas, for a particular partition z , can be calculated as

$$\bar{H}_z = \bar{C}_p (T_{G,z} - T_{\text{ref}}), \quad (34)$$

where \bar{C}_p is the gas molar heat capacity at constant pressure and T_{ref} is the temperature of reference for the enthalpy calculation, which is set to² 298.15 K.

Heat flow from the solid to the gas \dot{Q}_{SG} . The value of this structural parameter is estimated through a typical Newton's law of cooling expression, namely,

$$\dot{Q}_{SG} = UA_{HT} (T_S - T_G), \quad (35)$$

with U being the overall heat transfer coefficient, A_{HT} being the heat transfer area, and T_S being the temperature of the solid comprising the walls of the SSMR, which is assumed to be constant and uniform along the device.

4. Model simulation and validation

This section concludes the PBSM methodology by providing steps 8 to 10.

²In this paper, all enthalpy values are expressed relative to the standard reference temperature of 298.15 K, corresponding to the conventional thermodynamic reference state.

Table 2. Model constitutive and assessment equations.

Description	Constitutive/assessment equation	Units
1st equilibrium parameter in (25)	$\alpha_1 = 7.96$	-
2nd equilibrium parameter in (25)	$\beta_1 = 5.82$	bar ⁻¹
Total gas pressure	$P_G = \text{Datum} \geq 1 \times 10^5$	Pa
Membrane thickness	$\delta = 3 \times 10^{-5}$	m
Membrane surface area	$\alpha = \pi D_m (L_2/n)$	m ²
Membrane diameter	$D_m = 0.003175$	m
Length of separation stage	$L_2 = 0.076$	m
Number of partitions	$n = 50$	-
Partial pressure of hydrogen at retentate side	$p_{H,r} = p_H$	Pa
Partial pressure of hydrogen at permeate side	$p_{H,p} = \text{Datum}$	Pa
Pre-exponential factor of membrane permeability	$P_{e,0} = 1.35 \times 10^{-6}$	mol/(m min Pa ^{1/2})
Activation energy of membrane	$E_{am} = 8.8 \times 10^3$	J/mol
Pre-exponential factors of reaction kinetics	$k_{\infty,1} = 2.1 \times 10^4$ $k_{\infty,2} = 2.0 \times 10^3$ $k_{\infty,3} = 1.9 \times 10^4$ $k_{\infty,4} = 2.0 \times 10^5$	-
Activation energies of reaction kinetics	$E_{a,1} = 7.0 \times 10^4$ $E_{a,2} = 1.3 \times 10^5$ $E_{a,3} = 7.0 \times 10^4$ $E_{a,4} = 9.8 \times 10^4$	J/mol
Average molar heat capacity at constant volume	$\bar{C}_v = \bar{C}_p - R$	J/(mol K)
Average molar heat capacity at constant pressure	$\bar{C}_p = \sum_{i=E}^M y_i \bar{C}_{p,i}$	J/(mol K)
Molar heat capacities at constant pressure	$\bar{C}_{p,i}$ = polynomial expressions in terms of T_G taken from [44]	J/(mol K)
Molar enthalpy of reactions	$\Delta \bar{H}_{\text{rxn},j} = \Delta \bar{H}_{\text{rxn},j}^{\circ} + \Delta \bar{C}_{p,j} (T_G - T_{\text{ref}})$	J/mol
Standard enthalpy of reactions	$\Delta \bar{H}_{\text{rxn},1}^{\circ} = 63300$ $\Delta \bar{H}_{\text{rxn},2}^{\circ} = 48970$	J/mol

Description	Constitutive/assessment equation	Units
	$\Delta \bar{H}_{\text{rxn},3}^{\circ} = -41180$ $\Delta \bar{H}_{\text{rxn},4}^{\circ} = 109080$	
Difference between heat capacity of products and reactants	$\Delta \bar{C}_{p,1} = \bar{C}_{p,H} + \bar{C}_{p,A} - \bar{C}_{p,E}$ $\Delta \bar{C}_{p,2} = \bar{C}_{p,H} + \bar{C}_{p,M} + \bar{C}_{p,CM} - \bar{C}_{p,E}$ $\Delta \bar{C}_{p,3} = \bar{C}_{p,H} + \bar{C}_{p,CD} - \bar{C}_{p,W} - \bar{C}_{p,CM}$ $\Delta \bar{C}_{p,4} = 5\bar{C}_{p,H} + 2\bar{C}_{p,CD} - 3\bar{C}_{p,W} - \bar{C}_{p,A}$	J/(mol K)
Overall heat transfer coefficient	$U = C_1 1500$	J/(min m ² K)
Correction factor as a function of P_G (in Pa)	$C_1 = -1 \times 10^{-24} P_G^4 + 3 \times 10^{-18} P_G^3$ $-2 \times 10^{-12} P_G^2 + 4 \times 10^{-7} P_G + 0.1095$	-
Area of heat transfer	$A_{HT} = \pi D_c (L_1/n)$	m ²
Diameter of one channel	$D_c = 1.2 \times 10^{-3}$	m
Length of reforming stage	$L_1 = 0.154$	m
Hydrogen molar enthalpy	$\bar{H}_H = \bar{C}_{p,H} (T_G - T_{\text{ref}})$	J/mol

4.1. Step 8. Degrees of freedom analysis

This step verifies the degrees of freedom (DoF) of the extended structure of the model. The DoF are defined as the difference between the number of quantities to be determined and the number of equations. For a model to be effectively simulated, the DoF must be zero. However, for a specific PS they may differ from zero, indicating information exchange with other PSs. In this case, there are 19 variables, 25 structural parameters, and 55 functional parameters. Thus, the number of quantities to be determined is 99. Accordingly, the model consists of 99 equations: 19 ordinary differential equations and 80 algebraic equations.

4.2. Step 9. Computational model construction

The computational model is implemented as a Python-based program capable of simultaneously and efficiently solving the complete set of model equations. In this study, the model was developed using the `solve_ivp` function from the `scipy.integrate` module. Given the system's complexity and stiffness, the backward differentiation formula (BDF) method was employed. Such a method is a variable-order, implicit multi-step technique well-suited

for stiff differential equations. The complete computational model is freely available through an online repository.³

4.3. Step 10. Model validation

The experimental procedure was based on the methodology reported in [45], with adaptations to the current system configuration, i.e., a liquid ethanol/water mixture, prepared to achieve a specified steam-to-carbon (S/C) ratio, is delivered from a storage tank using a Smartline[®] pump (Knauer Wissenschaftliche Geräte GmbH, Berlin, Germany). The mixture is vaporized in a heated line prior to entering the SSMR, reaching thermal equilibrium with the device walls. The temperature of the device walls is maintained constant by an electrical resistance heater controlled by a proportional–integral–derivative (PID) controller (PXR4, Fuji Electric Co., Tokyo, Japan) and insulated with glass wool. A K-type thermocouple in direct contact with the membrane surface provides precise temperature monitoring.

On the retentate side, a liquid trap condenses and collects any non-gaseous species, while pressure is manually regulated with a back-pressure valve to allow operation under different steady-state pressures. The permeate side remains open to the atmosphere without additional pressure control. Gas compositions from both streams are analyzed online using an Agilent 3000 A MicroGC (Agilent Technologies, Santa Clara, CA, USA) equipped with MS 5 Å, Plot U, and Stabilwax columns. The hydrogen flow rate on the permeate side is measured with a Bronkhorst electronic mass flow meter, and the retentate volumetric flow rate with a soap-bubble meter. A series of steady-state experiments are performed by varying the gas pressure while keeping inlet flows, S/C ratio, inlet gas temperature, walls temperature, and catalyst load constant. Each condition is maintained until steady state is confirmed from stable chromatographic concentration profiles.

Model validation was performed by comparing simulation results with experimental data under identical inlet conditions, namely a S/C ratio of 2.4, a temperature of 500°C, and different operating pressures. This S/C ratio corresponds to an inlet ethanol molar flow of 0.0021 mol/min and an inlet water molar flow of 0.0099 mol/min. Two additional parameters, referred to as correction factors C_2 and C_3 , were incorporated into the computational model to refine the reaction kinetics and ensure consistency in the energy

³To be provided after the manuscript revision.

balance. Together with the previously defined parameter C_1 , these factors were estimated by solving a sequential quadratic programming (SQP) problem designed to minimize the sum of squared errors across molar flows of multiple species, thereby formulating the calculation as a multiobjective optimization problem. These three parameters were formulated as a function of the operating pressure.

The validation results shown in Fig. 4 demonstrate suitable agreement between the simulation and experimental values of outlet steady-state molar flows, with the adjusted parameters effectively capturing the experimental trends across different operating pressures. Likewise, Fig. 5 presents the results of model validation at different gas inlet temperatures, with the gas pressure held constant at 800 kPa. The simulation results show appropriate agreement with the experimental trends.

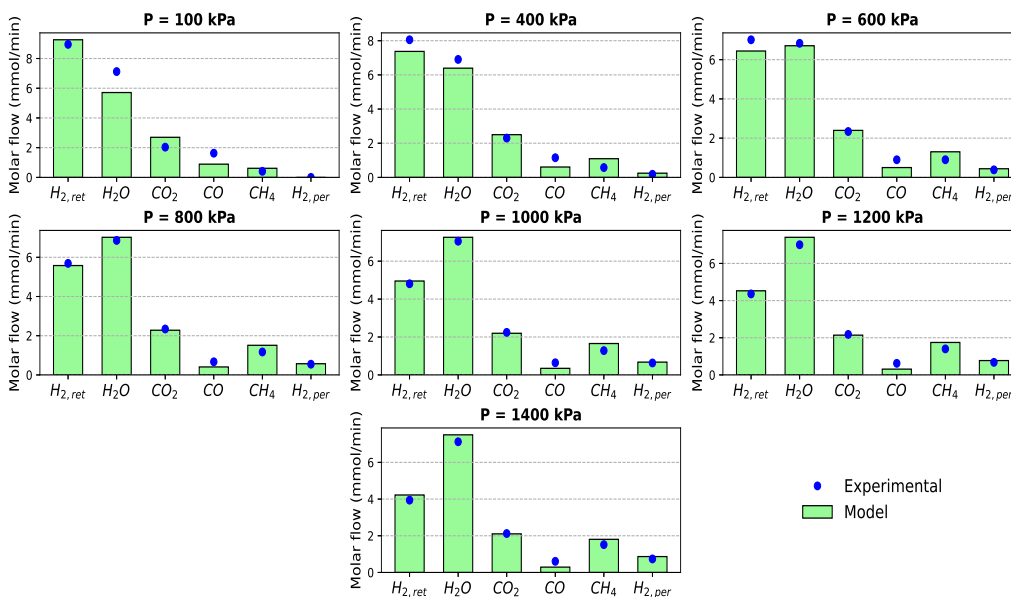


Fig. 4. Simulated and experimental outlet molar flows at different operating pressures. Hydrogen is shown for both retentate and permeate sides. Ethanol and acetaldehyde are omitted as they are fully consumed.

The experimental setup is in its early stage of development and can be further optimized in terms of both design and operating conditions. This fact is reflected in the relatively low pure hydrogen production efficiency and the limited portion of the reactor effectively utilized for chemical reactions, as shown by the steady-state molar flow profiles of all species in Fig 6. These ob-

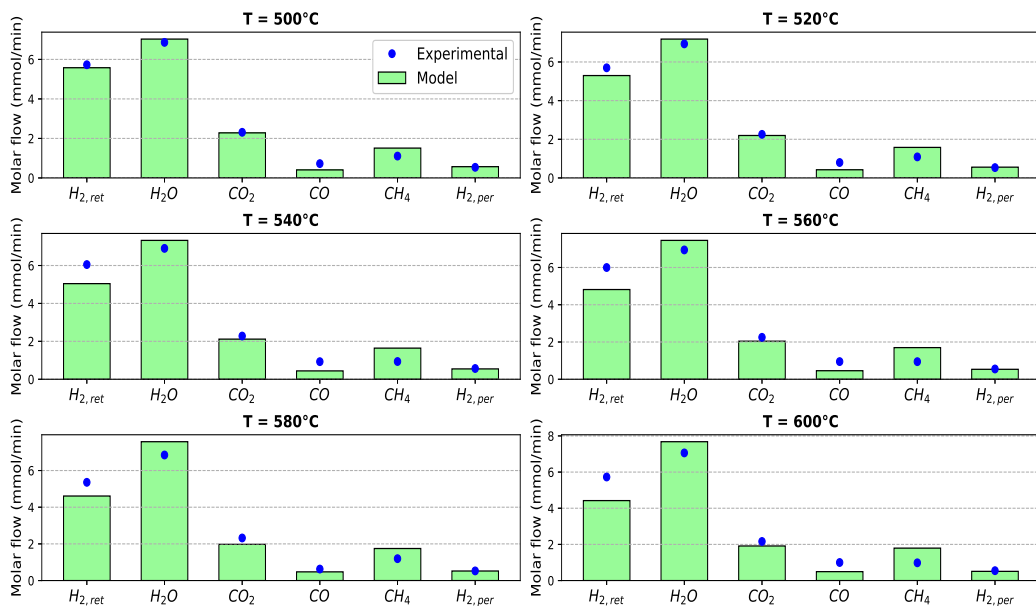


Fig. 5. Simulated and experimental outlet molar flows at different gas inlet temperatures. Hydrogen is shown for both retentate and permeate sides. Ethanol and acetaldehyde are omitted as they are fully consumed.

servations highlight a key application of the model: supporting the required optimization of equipment design and operation.

Distributed experimental measurements of temperature and gas composition along the reactor axis are not available for the present system. Obtaining such axial profiles would require the installation of multiple thermocouples and gas composition sensors, which is technically complex, costly, and may significantly disturb the hydrodynamics, heat transfer, and mass transport within the reactor. For this reason, and in line with common experimental practice for similar reactors, temperature and composition are measured only at the reactor outlet [46, 47, 48]. The pressure drop is assumed negligible due to the short reactor length, low gas velocities, and laminar flow operation. Although experimental axial profiles are not available, the model is derived from first principles, and rigorously enforces mass conservation. Consequently, the predicted axial distributions of temperature and species composition follow physically consistent and well-established trends for this type of reactors.

On the other hand, Fig. 7 shows the dynamic behavior of the key product of interest in the process: the molar flow of pure hydrogen exiting PS III.

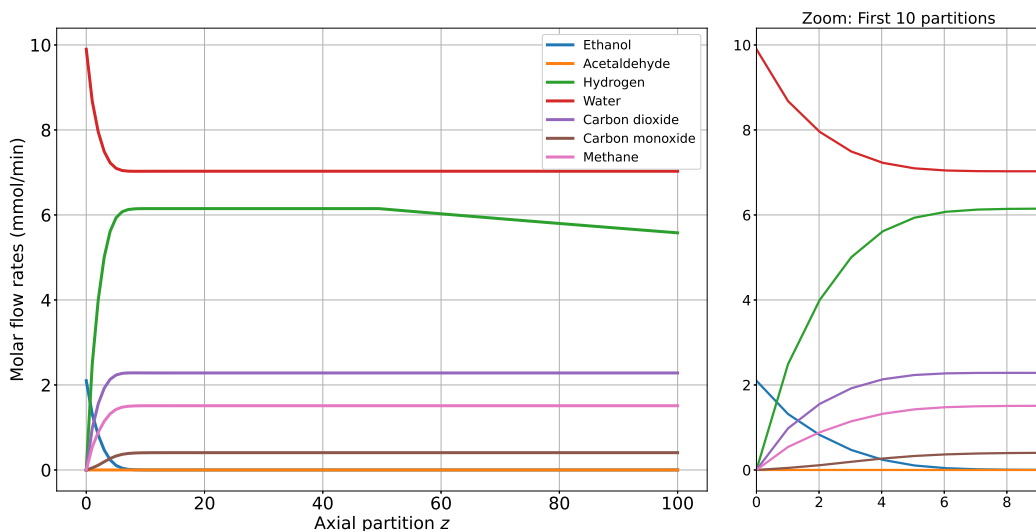


Fig. 6. Steady-state molar flows of all species. Operating conditions: inlet ethanol flow of 0.0021 mol/min, inlet water flow of 0.0099 mol/min, gas inlet temperature of 500°C and gas pressure of 800 kPa. Partitions from 0 to 50 correspond to PS I and partitions from 51 to 100 correspond to PS II.

The results correspond to the system’s response to a 10% step increase in the inlet gas pressure and the inlet gas temperature. The nominal operating conditions were an inlet ethanol flow of 0.0021 mol/min, an inlet water flow of 0.0099 mol/min, a pressure of 400 kPa, and an inlet gas temperature of 500°C. The results indicate that the pure hydrogen flow is more sensitive to pressure disturbances than to temperature variations, exhibiting a faster and larger response to changes in inlet pressure due to the direct dependence of membrane permeation on hydrogen partial pressure. In contrast, although a large inlet temperature step is applied, the constant reactor wall temperature attenuates the thermal disturbance, resulting in a smaller change in hydrogen flow.

5. Conclusions

This article presented the development and validation of a nonlinear dynamic model for the ethanol steam reforming (ESR) process in a staged-separation membrane reactor (SSMR), derived using the phenomenological-based semi-physical modeling (PBSM) methodology. The proposed model integrates the reforming and hydrogen separation stages within a single unit,

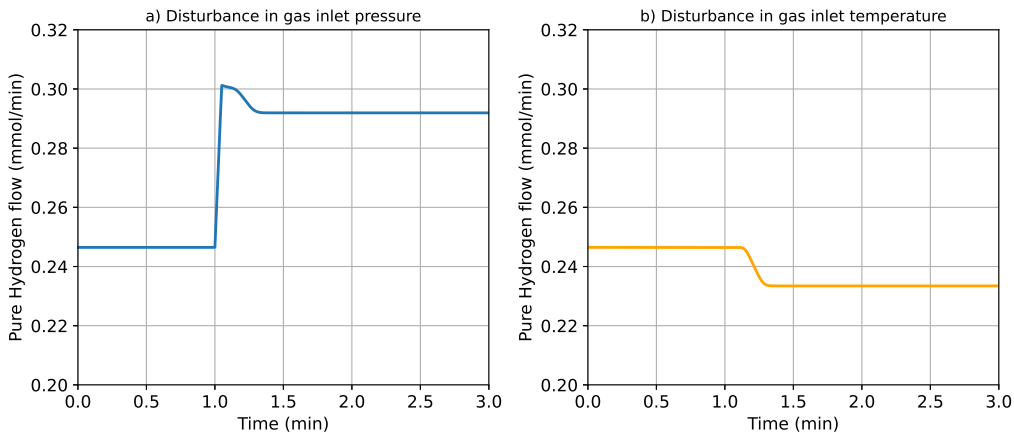


Fig. 7. Dynamic response of the pure hydrogen molar flow to *a)* a 10% step increase in the inlet gas pressure at the retentate side and *b)* a 10% step increase in the inlet gas temperature. In both cases, the disturbance was introduced at 1.0 minutes of simulation time.

capturing the coupled mass and energy transport phenomena that determine the system’s dynamic behavior.

The PBSM approach enabled the systematic formulation of an interpretable and modular model structure, where most parameters are directly linked to physical quantities or process characteristics. This modularity allows the model to be easily extended or simplified as new information becomes available or as the modeling objectives evolve. Model parameters were identified through a multi-objective optimization algorithm using experimental data from a real SSMR setup. The resulting model showed suitable agreement with experimental results under various operating conditions, demonstrating its accuracy and reliability.

Simulation results provided valuable insights into the process’s sensitivity to key operating variables, such as pressure and inlet temperature, which are critical for performance optimization and control strategy design. The computational model was implemented in Python and made openly available, promoting reproducibility and further research in process modeling, optimization, and control of SSMRs for hydrogen production.

The developed model represents a relevant tool for the analysis, design, and optimization of ESR systems. Future work will focus on model-based optimization, control applications, and the incorporation of additional physical phenomena.

Appendix A. Mass transfer limitation

In this appendix, a relevant discussion on potential mass transfer limitations is presented. For chemical reactions to occur within the reactor, reactants must diffuse from the bulk gas phase to the catalytic surface along the monolith walls. A potential concern arises when mass transfer limitations prevent reactants from effectively reaching the catalyst, thereby preventing the reaction kinetics from achieving their expected rates. In other words, depending on the relative rates of mass transfer and the chemical reaction, one of the two becomes the limiting step, ultimately determining the overall reaction rate. For each partition z , the limiting step can be identified using the first Damköhler number, which, in this work, is defined for the case of ethanol mass transfer as follows:

$$Da_I = \frac{r_1 + r_2}{\dot{n}_{MT,E}}, \quad (\text{A.1})$$

where r_1 and r_2 are the rates of reactions (1) and (2), respectively, and $\dot{n}_{MT,E}$ is the molar flow rate of ethanol from the bulk gas to the catalytic surface due to mass transfer, which is calculated as follows:

$$\dot{n}_{MT,E} = A_{MT} k_{bulk} (C_{E,1} - C_{E,2}), \quad (\text{A.2})$$

with A_{MT} being the mass transfer area, k_{bulk} being the bulk gas mass transfer coefficient, and $C_{E,1}$ and $C_{E,2}$ being the ethanol concentrations at points 1 and 2 shown in Fig. A.1, respectively. The concentration $C_{E,1}$ is directly obtained from the model equations through the ethanol mole fraction $y_{E,z}$, as follows:

$$C_{E,1} = \frac{y_{E,z} P_G}{R T_{G,z}}, \quad (\text{A.3})$$

where P_G is the total gas pressure, $T_{G,z}$ is the gas temperature, and R is the gas universal constant. In contrast, $C_{E,2}$ must be determined using a different equation, for instance, by applying a mass conservation relationship such as

$$k_{layer} (C_{E,2} - C_{E,3}) = k_{bulk} (C_{E,1} - C_{E,2}),$$

where k_{layer} is the boundary layer mass transfer coefficient and $C_{E,3}$ is the ethanol concentration at point 3. Assuming enough fast reaction rates, $C_{E,3}$

can be considered negligible for the reactants, and therefore

$$C_{E,2} = \frac{k_{bulk}}{k_{layer} + k_{bulk}} C_{E,1}. \quad (\text{A.4})$$

Although point 4 is depicted within the catalytic surface pores for completeness, the mass transfer occurring inside the solid pores is not modeled, as it falls beyond the level of detail considered in this work.

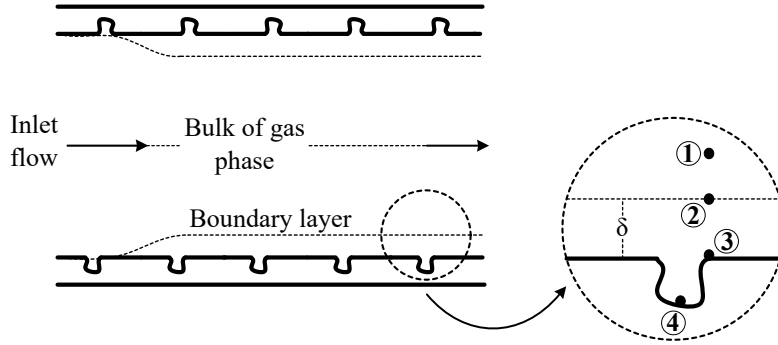


Fig. A.1. Key points for mass transfer calculation within the channel in the reforming stage.

Since the concentration boundary layer theory assumes that the fluid within the layer is stationary, mass transfer occurs purely by diffusion. Hence, the mass transfer coefficient of the layer can be calculated as

$$k_{layer} = \frac{\mathcal{D}_E}{\delta_c}, \quad (\text{A.5})$$

where \mathcal{D}_E represents the ethanol diffusivity in water and δ_c denotes the concentration boundary layer thickness, which can be estimated as

$$\delta_c = \text{Sc}^{-\frac{1}{3}} \sqrt{\frac{12 \nu x}{v_\infty}}, \quad (\text{A.6})$$

with Sc being the Schmidt number, ν being the kinematic viscosity, x being the distance downstream from the start of the boundary layer, and v_∞ being the bulk gas velocity. The Schmidt number is defined as

$$\text{Sc} = \frac{\mu}{\rho \mathcal{D}_E}, \quad (\text{A.7})$$

where μ and ρ are the gas viscosity and density, respectively.

On the other hand, the bulk gas mass transfer coefficient must be obtained by using a suitable correlation, as the following sequence of calculations proposed in [49]:

$$k_{bulk} = \frac{\text{Sh } \mathfrak{D}_E}{L_c}, \quad (\text{A.8})$$

$$\text{Sh} = 2 + 0.552 \text{Re}^{1/2} \text{Sc}^{1/3}, \quad (\text{A.9})$$

$$\text{Re} = \frac{\rho v_\infty L_c}{\mu}, \quad (\text{A.10})$$

where Sh and Re represent the dimensionless Sherwood and Reynolds numbers, respectively, and L_c is the characteristic length.

References

- [1] T. Ahmad, D. Zhang, A critical review of comparative global historical energy consumption and future demand: The story told so far, *Energy Reports* 6 (2020) 1973–1991. doi:<https://doi.org/10.1016/j.egy.2020.07.020>.
- [2] IEA. *Global Energy Review* [online] (2025).
- [3] M. Filonchyk, M. P. Peterson, L. Zhang, V. Hurynovich, Y. He, Greenhouse gases emissions and global climate change: Examining the influence of CO₂, CH₄, and N₂O, *Science of The Total Environment* 935 (2024) 173359. doi:<https://doi.org/10.1016/j.scitotenv.2024.173359>.
- [4] S. Bakhsh, W. Zhang, K. Ali, J. Oláh, Strategy towards sustainable energy transition: The effect of environmental governance, economic complexity and geopolitics, *Energy Strategy Reviews* 52 (2024) 101330. doi:<https://doi.org/10.1016/j.esr.2024.101330>.
- [5] Q. Hassan, S. Algburi, A. Z. Sameen, T. J. Al-Musawi, A. K. Al-Jiboory, H. M. Salman, B. M. Ali, M. Jaszczur, A comprehensive review of international renewable energy growth, *Energy and Built Environment* (2024). doi:<https://doi.org/10.1016/j.enbenv.2023.12.002>.
- [6] M. Sohaib, A. Majeed, J. Liu, J. Oláh, The role of renewable energy in mitigating carbon emissions: Insights from china’s energy

- consumption patterns, *Energy Strategy Reviews* 61 (2025) 101860. doi:<https://doi.org/10.1016/j.esr.2025.101860>.
- [7] S. K. Suraparaju, M. Samykano, J. R. Vennapusa, R. K. Rajamony, D. Balasubramanian, Z. Said, A. K. Pandey, Challenges and perspectives of energy storage integration in renewable energy systems for net zero transition, *Journal of Energy Storage* 125 (2025) 116923. doi:<https://doi.org/10.1016/j.est.2025.116923>.
- [8] M. Yue, H. Lambert, E. Pahon, R. Roche, S. Jemei, D. Hissel, Hydrogen energy systems: A critical review of technologies, applications, trends and challenges, *Renewable and Sustainable Energy Reviews* 146 (2021) 111180. doi:<https://doi.org/10.1016/j.rser.2021.111180>.
- [9] M. M. Hossain Bhuiyan, Z. Siddique, Hydrogen as an alternative fuel: A comprehensive review of challenges and opportunities in production, storage, and transportation, *International Journal of Hydrogen Energy* 102 (2025) 1026–1044. doi:<https://doi.org/10.1016/j.ijhydene.2025.01.033>.
- [10] S. Algburi, O. Al-Dulaimi, H. F. Fakhruldeen, D. H. Khalaf, R. N. Hanoon, F. I. Jabbar, Q. Hassan, A. K. Al-Jiboory, S. Kiconco, The green hydrogen role in the global energy transformations, *Renewable and Sustainable Energy Transition* 8 (2025) 100118. doi:<https://doi.org/10.1016/j.rset.2025.100118>.
- [11] M. SaberiKamarposhti, H. Kamyab, S. Krishnan, M. Yusuf, S. Rezanian, S. Chelliapan, M. Khorami, A comprehensive review of AI-enhanced smart grid integration for hydrogen energy: Advances, challenges, and future prospects, *International Journal of Hydrogen Energy* 67 (2024) 1009–1025. doi:<https://doi.org/10.1016/j.ijhydene.2024.01.129>.
- [12] S. Evro, B. A. Oni, O. S. Tomomewo, Carbon neutrality and hydrogen energy systems, *International Journal of Hydrogen Energy* 78 (2024) 1449–1467. doi:<https://doi.org/10.1016/j.ijhydene.2024.06.407>.
- [13] P. Afanasev, A. Askarova, T. Alekhina, E. Popov, S. Markovic, A. Mukhametdinova, A. Cheremisin, E. Mukhina, An overview of hydrogen production methods: Focus on hydrocarbon feedstock, *International Journal of Hydrogen Energy* 78 (2024) 805–828. doi:<https://doi.org/10.1016/j.ijhydene.2024.06.369>.

- [14] M. Rasul, M. Hazrat, M. Sattar, M. Jahirul, M. Shearer, The future of hydrogen: Challenges on production, storage and applications, *Energy Conversion and Management* 272 (2022) 116326. doi:<https://doi.org/10.1016/j.enconman.2022.116326>.
- [15] U. S. Behera, B. K. Purohit, H.-S. Byun, A comprehensive review of fossil-based hydrogen production: Technological integrations, environmental sustainability, and economic viability, *International Journal of Hydrogen Energy* 140 (2025) 627–652. doi:<https://doi.org/10.1016/j.ijhydene.2025.05.300>.
- [16] Z. Gholami, F. Gholami, J. Šimek, K. Svobodová, M. Vakili, Hydrogen production for a decarbonized future: a review of production technologies, *Journal of Industrial and Engineering Chemistry* (2025). doi:<https://doi.org/10.1016/j.jiec.2025.07.047>.
- [17] A. Al-Douri, K. M. Groth, Hydrogen production via electrolysis: State-of-the-art and research needs in risk and reliability analysis, *International Journal of Hydrogen Energy* 63 (2024) 775–785. doi:<https://doi.org/10.1016/j.ijhydene.2024.03.188>.
- [18] J. Yang, T. Y. Lam, Z. Luo, Q. Cheng, G. Wang, H. Yao, Renewable energy driven electrolysis of water for hydrogen production, storage, and transportation, *Renewable and Sustainable Energy Reviews* 218 (2025) 115804. doi:<https://doi.org/10.1016/j.rser.2025.115804>.
- [19] R. A. Abdelsalam, M. Mohamed, H. E. Farag, E. F. El-Saadany, Green hydrogen production plants: A techno-economic review, *Energy Conversion and Management* 319 (2024) 118907. doi:<https://doi.org/10.1016/j.enconman.2024.118907>.
- [20] B. Amini Horri, H. Ozcan, Green hydrogen production by water electrolysis: Current status and challenges, *Current Opinion in Green and Sustainable Chemistry* 47 (2024) 100932. doi:<https://doi.org/10.1016/j.cogsc.2024.100932>.
- [21] F. M. Mohsen, H. M. Mjbel, A. F. Challoob, R. Alkhazaleh, A. Alahmer, Advancements in green hydrogen production: A comprehensive review of prospects, challenges, and innovations in electrolyzer technologies, *Fuel* 404 (2026) 136251. doi:<https://doi.org/10.1016/j.fuel.2025.136251>.

- [22] A. Baig, Sonal, Steam reforming of methanol, ethanol, acetic acid, acetone, and bio-oil for hydrogen generation: Catalytic and mechanistic insight, *Bioresource Technology Reports* 28 (2024) 101980. doi:<https://doi.org/10.1016/j.biteb.2024.101980>.
- [23] W. M. Liew, N. Ainirazali, Cutting-edge innovations in bio-alcohol reforming: Pioneering pathways to high-purity hydrogen: A review, *Energy Conversion and Management* 326 (2025) 119463. doi:<https://doi.org/10.1016/j.enconman.2024.119463>.
- [24] A. H. Mohammed Abbas, K. K. Cheralathan, E. Porpatham, S. K. Arumugam, Hydrogen generation using methanol steam reforming – catalysts, reactors, and thermo-chemical recuperation, *Renewable and Sustainable Energy Reviews* 191 (2024) 114147. doi:<https://doi.org/10.1016/j.rser.2023.114147>.
- [25] E. Aguirre-Zapata, L. Lema-Perez, L. Gomez-Echavarria, H. Botero-Castro, J. C. Maya, F. Chejne, H. Alvarez, Useful properties of phenomenological-based models, *Ecological Modelling* 496 (2024) 110850. doi:<https://doi.org/10.1016/j.ecolmodel.2024.110850>.
- [26] A. Desgagnés, O. Alizadeh Sahraei, M. C. Iliuta, Improvement strategies for Ni-based alcohol steam reforming catalysts, *Journal of Energy Chemistry* 86 (2023) 447–479. doi:<https://doi.org/10.1016/j.jechem.2023.07.011>.
- [27] H. Gasparetto, N. P. G. Salau, A review on ethanol steam reforming focusing on yttria-stabilized zirconia catalysts: A look into hydrogen production for fuel cells, *Fuel* 371 (2024) 132140. doi:<https://doi.org/10.1016/j.fuel.2024.132140>.
- [28] M. A. Achomo, A. Kumar, N. R. Peela, P. Muthukumar, Hydrogen production from steam reforming of methanol: A comprehensive review on thermodynamics, catalysts, reactors, and kinetic studies, *International Journal of Hydrogen Energy* 58 (2024) 1640–1672. doi:<https://doi.org/10.1016/j.ijhydene.2024.01.159>.
- [29] M. Sariyer, N. A. Sezgi, T. Doğu, Process intensification methods in steam reforming of ethanol with nickel impregnated mesoporous carbon: Microwave heating and sorption enhanced reform-

- ing, *International Journal of Hydrogen Energy* 67 (2024) 912–924. doi:<https://doi.org/10.1016/j.ijhydene.2024.01.298>.
- [30] A. Bakhtyari, R. Bardool, M. R. Rahimpour, M. Mofarahi, C.-H. Lee, Performance analysis and artificial intelligence modeling for enhanced hydrogen production by catalytic bio-alcohol reforming in a membrane-assisted reactor, *Chemical Engineering Science* 268 (2023) 118432. doi:<https://doi.org/10.1016/j.ces.2022.118432>.
- [31] A. Cifuentes, R. Torres, J. Llorca, Modelling of the ethanol steam reforming over Rh-Pd/CeO₂ catalytic wall reactors, *International Journal of Hydrogen Energy* 45 (49) (2020) 26265–26273. doi:<https://doi.org/10.1016/j.ijhydene.2019.11.034>.
- [32] X. Yang, S. Wang, B. Li, Y. He, H. Liu, Performance of ethanol steam reforming in a membrane-assisted packed bed reactor using multiscale modelling, *Fuel* 274 (2020) 117829. doi:<https://doi.org/10.1016/j.fuel.2020.117829>.
- [33] J. Chen, Y. Yu, Numerical modelling for design of microchannel reactors: Application to hydrogen production from methanol by steam reforming, *International Journal of Hydrogen Energy* 50 (2024) 1526–1540. doi:<https://doi.org/10.1016/j.ijhydene.2023.11.061>.
- [34] S. Liu, P. Du, H. Jia, Q. Zhang, L. Hao, Study on the impact of methanol steam reforming reactor channel structure on hydrogen production performance, *Renewable Energy* 228 (2024) 120612. doi:<https://doi.org/10.1016/j.renene.2024.120612>.
- [35] W. H. Chen, W. S. Chou, S. Rajendran, S. Y. Hsu, M. Ghorbani, Hydrogen production and geometry optimization of ethanol steam reforming combining water gas shift reaction in a crossflow membrane tube reactor, *International Journal of Hydrogen Energy* 51 (2024) 637–653. doi:<https://doi.org/10.1016/j.ijhydene.2023.08.153>.
- [36] H. Alvarez, Phenomenological-based semi-physical models, formalizing the tool, in: S. Chakraborty, S. Curcio (Eds.), *Advanced Modelling and Simulation in the Chemical and Biochemical Process Industry*, CRC Press, Boca Raton, Florida, EEUU, 2024, pp. 43–71.

- [37] L. Lema-Perez, J. Garcia-Tirado, C. Builes-Montaño, H. Alvarez, Phenomenological-based model of human stomach and its role in glucose metabolism, *Journal of Theoretical Biology* 460 (2019) 88–100. doi:<https://doi.org/10.1016/j.jtbi.2018.10.024>.
- [38] H. Alvarez, C. Ocampo-Martinez, A phenomenological-based dynamic model for a polymer electrolyte membrane fuel-cell humidifier assembly, *Journal of Power Sources* 547 (2022) 231985. doi:<https://doi.org/10.1016/j.jpowsour.2022.231985>.
- [39] V. Freger, Solution-diffusion-mechanics model: Derivation, generalization, and non-equivalence of molecular simulations and experiments, *Journal of Membrane Science* 734 (2025) 124360. doi:<https://doi.org/10.1016/j.memsci.2025.124360>.
- [40] K. Hangos, I. T. Cameron, *Process modelling and model analysis*, Vol. 4, Academic Press, United States of America, 2001.
- [41] L. Lema-Perez, R. Muñoz-Tamayo, J. Garcia-Tirado, H. Alvarez, On parameter interpretability of phenomenological-based semiphysical models in biology, *Informatics in Medicine Unlocked* 15 (2019) 100158. doi:<https://doi.org/10.1016/j.imu.2019.02.002>.
- [42] I. Uriz, G. Arzamendi, E. López, J. Llorca, L. Gandía, Computational fluid dynamics simulation of ethanol steam reforming in catalytic wall microchannels, *Chemical Engineering Journal* 167 (2) (2011) 603–609, special Issue - IMRET 11: 11th International Conference on Microreaction Technology. doi:<https://doi.org/10.1016/j.cej.2010.07.070>.
- [43] R. Koch, E. López, N. J. Divins, M. Allué, A. Jossen, J. Riera, J. Llorca, Ethanol catalytic membrane reformer for direct PEM FC feeding, *International Journal of Hydrogen Energy* 38 (14) (2013) 5605–5615. doi:<https://doi.org/10.1016/j.ijhydene.2013.02.107>.
- [44] D. Green, R. Perry, *Perry's Chemical Engineers' Handbook*, Eighth Edition, McGraw Hill professional, McGraw Hill LLC, 2007.
- [45] A. Cifuentes, L. Soler, R. Torres, J. Llorca, Methanol steam reforming over PdZn/ZnAl₂O₄/Al₂O₃ in a catalytic membrane reactor: An experimental and modelling study, *Interna-*

- tional Journal of Hydrogen Energy 47 (22) (2022) 11574–11588. doi:<https://doi.org/10.1016/j.ijhydene.2022.01.186>.
- [46] X. Song, Z. Bao, Y. Jiao, Numerical simulation of ethanol steam reforming on structured SiC foam catalyst with direct electrical heating, Fuel 396 (2025) 135332. doi:<https://doi.org/10.1016/j.fuel.2025.135332>.
- [47] L. Qin, B. Jeon, K. Park, X. Tong, A. A. Matarru, H.-Y. Park, D. Shin, Development of dynamic modeling for ethanol reformer design and operation, International Journal of Hydrogen Energy 200 (2026) 152492. doi:<https://doi.org/10.1016/j.ijhydene.2025.152492>.
- [48] R. Ma, B. Castro-Dominguez, I. P. Mardilovich, A. G. Dixon, Y. H. Ma, Experimental and simulation studies of the production of renewable hydrogen through ethanol steam reforming in a large-scale catalytic membrane reactor, Chemical Engineering Journal 303 (2016) 302–313. doi:<https://doi.org/10.1016/j.cej.2016.06.021>.
- [49] S. Hafeez, E. Aristodemou, G. Manos, S. M. Al-Salem, A. Constantinou, Modelling of packed bed and coated wall microreactors for methanol steam reforming for hydrogen production, RSC Adv. 10 (2020) 41680–41692. doi:[10.1039/D0RA06834A](https://doi.org/10.1039/D0RA06834A).